MAGICal GRB 190114C: Implications of cutoff in the spectrum at sub-*GeV* energies

Vikas Chand[†,1,2], Partha Sarathi Pal,[1] Ankush Banerjee,[1] Vidushi Sharma[*,3] P. H. T. Tam[!,1] and Xinbo He[1]

[1] *School of Physics & Astronomy, Sun Yat Sen University, Guangzhou 510275, China*
[2] *Tata Institute of Fundamental Research, Mumbai, India*
[3] *Inter University Centre for Astronomy and Astrophysics, Pune, India*

ABSTRACT

GRB 190114C is an unusual gamma-ray burst (GRB) due to its detection at sub-*TeV* energies by MAGIC, seen at redshift z = 0.42. This burst is one of the brightest GRB detected by *Fermi* . A joint GBM-LAT analysis of the prompt emission reveals the presence of sub-*GeV* spectral cutoff when the LAT *low-energy events* (LLE) data is also examined. A similar high-energy cutoff was likewise reported in GRB 160509A and GRB 100724B earlier, as well as handful of other sources. The cutoff can be explained by the intrinsic opacity due to pair production within the emitting region. GRB 190114C shows a transition from non-thermal to a quasi-thermal-like spectrum and a radiation component that can be attributed to afterglow. Based on spectral analysis, we constrain the site of the prompt emission and *Lorentz* factor. Knowing that sub-*TeV* photons are detected in MAGIC, we perceive that the observed spectrum is indeed an overlap from two emission sites, where the emission observed in *Fermi* is more consistent with prompt emission produced via photospheric dissipation along with a concurrent component from the external shock.

Keywords: gamma-ray burst: GRB 190114C , GRB 160509A - radiation mechanisms: thermal, non-thermal - methods: data analysis

1. INTRODUCTION

Gamma-ray burst (GRB) prompt emission spectra are traditionally modeled by the Band function (Band et al. 1993). However, deviations from the Band function were observed and reported previously, such as the presence of an extra thermal component (Ryde 2005; Page et al. 2011; Guiriec et al. 2011), spectral breaks (Oganesyan et al. 2017a,b), a Band function with high-energy cutoff (Ackermann et al. 2013; Tang et al. 2015; Vianello et al. 2017), and multiple thermal + non-thermal components (Guiriec et al. 2015b,a, 2016; Basak & Rao 2015). Observational evidence, however, could be affected by selection effects. Two very different models are sometimes barely distinguishable when folded with the response of a detector (see, e.g., Zhang et al. 2016; Vianello et al. 2017; Burgess 2019). Time-resolved spectral analysis, though a very reliable method to understand the emission mechanism, has implementation lim-

its because of poor statistics. A break at low energy is seen in GRBs observed simultaneously in soft and hard X-rays in *Swift* and at low and high-energy bands in *Fermi* (Oganesyan et al. 2017c; Ravasio et al. 2019a). However, multiple components in this range are also observed (Basak & Rao 2013; Iyyani et al. 2013). The presence of a thermal component and its effect on the non-thermal spectral emission have also been studied (e.g., Li 2019a; Guiriec et al. 2011; Axelsson et al. 2012; Guiriec et al. 2013), and the thermal components are in general considered to be signatures of photospheric emission.

On the theoretical side, consensus is building over two contending models, photospheric emission (dissipative or non-dissipative) and synchrotron emission in many possible settings (see, Kumar & Zhang 2015 for a review). Recently, a synchrotron model from a cooling population of electrons was used to study the prompt emission of the GRBs. Most of the GRB spectra used in these studies are consistent with synchrotron cooling (Burgess et al. 2018; Oganesyan et al. 2019). Photospheric models are also used in some studies and can well explain the data well (Vurm & Beloborodov 2016;

[†]vikas.chand.physics@gmail.com

[*]vidushi@iucaa.in

[!]tanbxuan@mail.sysu.edu.cn

Vianello et al. 2017; Ahlgren et al. 2019; Acuner et al. 2020).

The sub-GeV radiation from the bright burst with a good count statistics can give important insights. The question of whether the $\sim 100\ MeV$ emission has an external shock origin or internal dissipation origin is still under debate (see Tang et al. 2015, and references therein). Time-dependent broadband model fits from keV to GeV energies can help us to distinguish these two origins. The spectral cutoffs, if observed, can also play a pivotal role in pinning down the site of the prompt emission production in GRBs (Gupta & Zhang 2008). The spectral cutoffs can also be decisively important in understanding the origin of the radiation and components of a GRB jet (Zhang & Pe'er 2009). Additionally, in the cases where both the external and internal dissipation is contributing to the $\sim 100\ MeV$ emission, model fits with short time slices (e.g., 1 s) can reveal the time evolution of both contributions as well as the transition from prompt emission to the afterglow emission phase.

With the *Fermi* space observatory, the broadband spectrum of the GRBs can be studied from a few keV up to hundreds of GeVs. Some bright bursts have shown bright emission in *Fermi* -LAT also, thus allowing enough photon statistics even in short time slices. GRB 160625B is one such example where the emission was seen in the sub-GeV LAT band. A joint analysis of the emission observed in the *Fermi* detectors shows a cutoff in the spectra in the $\sim 100\ MeV$ energy range (Wang et al. 2017). Similarly, GRB 160509A is yet another example. A break similar to GRB 160625B exists for this GRB and GRB 100724B (Vianello et al. 2017). A detailed analysis with LAT emission during the prompt emission can reveal that the contamination of the spectrum by lower energy components can lead to a dramatic evolution (discussed in Appendix B). GRB 190114C shows one bright pulse in the LAT. Several spectral studies of GRB 190114C have been performed (Wang et al. 2019, Ravasio et al. 2019b), but caveats of these works include: (a) separate analysis instead of joint analysis and (b) wider time bins being chosen while performing the spectral analysis. There are hints from these studies though that the initial part of the LAT spectrum could be affected by the prompt emission spectrum.

GRB 190114C , in its multiwavelength spectral energy density, showed evidence for a double-peaked distribution with the first peak being the synchrotron emission. The second peak shows a very high-energy (VHE) emission in TeV energies and is explained by the synchrotron self-Comptonization process, theoretically predicted in a standard afterglow model (MAGIC Collaboration et al.

2019). We present the evolution of the spectrum of the prompt emission by using joint GBM-LAT analysis, by trying several typical empirical spectral models. The observed sub-GeV cutoffs and the thermal components in the spectra are utilized to evaluate *Lorentz* factor (Γ) in various scenarios and also to constrain the site of the prompt emission (Lithwick & Sari 2001; Pe'er et al. 2007; Zhang & Pe'er 2009).

We summarize the major observations of GRB 190114C in Section 2. We draw a parallel of GRB 190114C with GRB 160509A and also demonstrate the transition of the LAT emission from prompt to afterglow for the later in Section 3. Results are presented and discussed in Sections 4 and 5, respectively. We also underline a systematic approach in Appendix B that can be followed to uncover a sub-GeV cutoff in the case of a simultaneous presence of external components.

2. OBSERVATIONS

GRB 190114C triggered the *Neil Gehrels Swift Observatory* - Burst Alert Telescope (BAT) at 20:57:03 UT ($T0$, trigger time), on 2019 January 14. Later, the optical counterpart was detected by several observatories in various bands, and with detection of absorption lines the redshift was found to be z = 0.4245 ± 0.0005 (Castro-Tirado et al. 2019). Surprisingly, MAGIC detected GRB 190114C in the sub-TeV energy domain starting at $T0 + 50\ s$. A clear excess of gamma ray events was detected with a significance of more than 20 σ within the first 20 minutes with energies of the photons greater than 300 GeV (Mirzoyan et al. 2019). The *Fermi* GBM light curve shows a bright, multipeaked pulses from $T0 + 0\ s$ to $T0 + 15\ s$ followed by a fainter emission lasting up to $T0 + 200\ s$. The calculated T90 (Koshut et al. 1995) duration of the light curve was found to be 116 s (within $50 - 300\ KeV$), along with an energy fluence (within $10 - 1000\ keV$) of $(3.99 \times 10^{-4} \pm 8.10 \times 10^{-7})\ erg\ cm^{-2}$ and the estimated isotropic energy release was $3 \times 10^{53}\ erg$. This source was also detected by AGILE/MCAL in the $0.4 - 100\ MeV$ energy band for a duration of 6.2 s (Ursi et al. 2019). As observed by *Konus-Wind*, the main burst showed a hard-spectrum multipeaked pulse starting from $T0$ to $T0 + 6\ s$ with a fluence of $(4.83 \pm 0.10) \times 10^{-4}\ erg\ cm^{-2}$ (Frederiks et al. 2019).

3. METHOD AND ANALYSIS

The data are obtained from the publicly available data archive on the *Fermi Science Support Center* (FSSC) [1]. The spectra were reduced using *Fermi science tools*

---

[1] https://fermi.gsfc.nasa.gov/ssc/

software `gtburst` by standard methodology[2]. For LAT, transient event class and its instrument response function `P8_TRANSIENT020` were used. The spectral analysis is performed in `XSPEC` (Arnaud 1996), and `pgstat` was used for testing various models since the data is Poissonian and background is Gaussian background as it is derived from modeling the data in off-source intervals by a polynomial [3]. Furthermore, to fit the different components of the spectrum we used the Band model (Band et al. 1993) (B) for one, and B + power law with a multiplicative cutoff component (B + CPL) for the other. A model with exponential cutoff applied to the Band model (BC) is also used (see section A for the forms of the functions used. To find which model fits the data best, we used the Bayesian Information Criterion (BIC) and the Akaike Information Criterion (AIC). Given their properties, AIC is preferred to compare nonnested models such as Band function, or power law. Whereas, BIC is preferred when nested models such as blackbody added to a band function are compared (Kass & Rafferty 1995). The change in AIC or BIC can predict the model with strong correlation to the data. All errors are presented within $1\ \sigma$ (68% nominal) confidence levels.

We take brighter GBM-NaI detectors with off-axis angles less than 50° and GBM-BGO covering the same hemisphere of spacecraft as NaI detectors. In case of GRB 190114C , we have considered NaI 3, 4, 7, 8 and BGO 0, 1 (n3, n4, n7, n8, b0 and b1). LAT data is also used (both LLE and $> 100\ MeV$ data). Here, we would be referring to energies $> 100\ MeV$ as LAT-HE. To account for inter-instrument calibration, we applied a multiplicative constant factor (effective area correction factor) w.r.t the detector having the highest count rate. The factor is allowed to vary up to $\sim$ 20 - 30% as the EAC constant factor is not expected to differ by more than 30%.

3.1. GRB 190114C

3.1.1. Joint GBM-LAT analysis

The energy range 8 - 900 keV was used for NaI detectors, $\sim$ 0.2 - 38 MeV was used for the BGO detectors, 20 - 100 MeV was used from LLE and $>100\ MeV$ was used for LAT-HE. We neglected $\sim$ 30 - 40 keV from our spectral analysis to exclude the 33.17 keV K-edge feature. In Fig. 1, we can observe that contrary to GRB 160509A , the initial emission in GRB 190114C is limited to the

1 - 30 MeV band only, however, the bright pulse during the peak finds its correspondence in the 30 - 100 MeV LLE band, and in LAT-HE only some photons with relatively low energies are observed. As in the case of GRB 160509A , the later emission can contaminate the prompt emission (See Appendix B for more details). The presence of the afterglow component could be felt prominently at low energies during the prompt emission. This component noticeably pollutes the prompt spectrum after 4.8 s (Ravasio et al. 2019b). Interestingly, the LAT photon index also shows soft to hard evolution (Wang et al. 2019) similar to GRB 160509A . We thus explore the joint GBM-LAT data for the possibility of a spectral cutoff in the prompt emission.

Looking at the light-curve morphology, it is intuitive that this cutoff, if present, will show considerable evolution as well as contamination from the afterglow. We resolve the spectrum using archived LLE data in 1 s bins. Interestingly, a fit to the Band function has a systematic trend in its residuals beyond 100 MeV, and this contrast is most prominent in the 3 - 4 s bin as shown in Fig 2. This could be regarded as the signature of a cutoff in the energy spectrum around this energy range. So we added a power-law component with an exponential cutoff. The added component returned a well-constrained cutoff $\sim$ 50 MeV at 3 - 4 s since the GBM trigger. The improvement in statistics strongly favors the addition of a cutoff power law. Alternatively, we modeled with BC, B + BB and BB + BC. BB + BC is strongly favoured among these; however, in comparison with B + CPL, the later is very strongly favored (ΔAIC = 45, ΔBIC = 44.4). So, it is evident that the high-energy data cannot be modeled by simply extrapolating the low-energy model and a cutoff is definitely required in the spectrum.

The cutoff during 4-5 s could not be well constrained for the upper bound. This is not surprising because of the rising contribution from the afterglow, which is significant after 4.8 s (Ravasio et al. 2019b). The low-energy spectrum becomes harder within 3 - 5 s. The Band model with an additional cutoff power law fits better in these bins as reflected by the large decrease in BIC and AIC. The spectra are shown in Fig 2. Taking energies above 10 MeV we confirm that `pgstat` with a cutoff power law has 20% and 18% contribution, respectively. For further confirmation of the cutoff, we just take the data above 10 MeV and model it by both power law and a multiplicative cutoff. The fit to power law resulted in a slope of $2.53^{+0.14}_{-0.13}$ along with `pgstat` and degree of freedom (dof)$= 107.2(72)$, and that to cutoff power law shows a cutoff at $60^{+70}_{-22}\ MeV$ with slope 1.5 ± 0.5 and `pgstat` (dof) $= 92(71)$. Thus, the feature could be recovered with ΔBIC = 10 which shows that

an energy cutoff is very strongly preferred over a simple power-law decay. We show the fits to both models in Fig 3, and also derive confidence contours for cutoff energy (E_c) and index (ξ) of the $\sim E^{-\xi} \exp(\text{-E}/E_c)$ function. The cutoff can be constrained well (Fig 3) and is also close to what is determined from the entire data fit in this interval.

3.1.2. *Further Time-resolved analysis*

We chose a signal-to-noise ratio of 50 (from n4). Time bins created in this manner are reported in Table 3. We chose models Band function (B), a blackbody added to band function (B + BB), a blackbody added to CPL (BB + CPL), a broken power-law model with two sharp breaks `bkn2pow` and a broken power law with sharp breaks and a cutoff (`bknpowC`). The formulas for all the models used are reported in the (Appendix A). We presented our results in Table 3. During 0.7 - 1.7 s, `bknpowC` describes the spectrum at par with BB + CPL. So, the blackbody fitted in Wang et al. (2019) can be modeled by a low-energy break. However, in the later phase the spectrum could be modeled by BB + Band. The spectra in the later phase are also modeled with a smoothly broken power law by Ravasio et al. (2019b), however, they also found the spectral index became harder during these times (2.45 - 5.69 s). Therefore, we can say that the spectrum is initially nonthermal with a low-energy cutoff (sub-MeV) which later becomes quasi-thermal.

4. RESULTS

We can calculate the *Lorentz* factor (Γ) if the cutoff thus obtained is attributed to the $\gamma - \gamma$ absorption (Lithwick & Sari 2001), denoted here by Γ_i (Table 2). For the photons that self-annihilate, the photon energy should be comparable to the cutoff energy E_c thus allowing us to estimate the bulk Γ (Lithwick & Sari 2001), denoted here by Γ_{ii}. When the Comptonization of the photons by the $e^- - e^+$ pairs produced by photon annihilation is also considered, the lower limit on the Γ (Lithwick & Sari 2001) is given by Γ_{iii}. Another limit on Γ may be obtained by considering the scattering of photons by electrons associated with baryons (Lithwick & Sari 2001), $\Gamma_{iv} > \hat{\tau}^{1/(-\beta+3)} \left[\hat{\tau}^{(-\beta-2)/(-\beta+3)} \times (E_p/m_p c^2)\right]^{1/5}$, where E_p is the peak energy of the Band function and $\hat{\tau}$ is defined in Table 2. However, since $E_p/m_p c^2$ is for our observed E_p values is $<< 1$, the above limit can be safely ignored. Among these Γs obtained by Γ_i to Γ_{iv}, the highest is the relevant one. A larger value of Γ is expected if the effect of Compton down-scattering on the cutoff energy in the comoving frame by the pair cascades is also considered (Gill & Granot 2018).

The various limits for the temporal bins where we could model a cutoff in the spectrum as an additional component (Table 1) are calculated and the results are presented in Table 2. We took the time bins for our calculations that have reasonable constraints on parameters. The most relevant constraints are during the 3 - 4 s time bin, where the cutoff energy $E_c/\sigma(E_c) \sim 5$, $\sigma(E_c)$ is the error in E_c. If the the emission was produced through synchrotron, then we can also estimate the limiting energy from synchrotron emission (*e.g.* Guilbert et al. 1983; de Jager & Harding 1992; Piran & Nakar 2010; Atwood et al. 2013), which can produce a cutoff energy feature using $E_{\text{syn,max}}$ defined in Table 2. Fraija et al. (2019), through multiband spectral and temporal analysis of the afterglow using forward and reverse shocks, along with the best-fit value of the circumburst density, estimated the value of the initial bulk Γ ($\Gamma_{0,ext}$) to be ~ 600. The Γ calculated from the sub-GeV cutoff is ~ 300, which is lower than the Γ obtained from the multi-wavelength analysis of the afterglows.

In the internal shock model, the shock radius is inferred from the minimum variability timescale ($R_{\text{IS}} \sim \Gamma^2 c\delta T$). However in some models, variability timescale may not be reflection of the central engine activity (Lyutikov & Blandford 2003; Narayan & Kumar 2009). For a given cutoff energy E_c, there exists a threshold energy E_{td}, above which the photons annihilate with the photons at energy E_c and produce pairs. The threshold energy is obtained by the condition where $(E_{\text{td}}/1 \text{ MeV})(E_c/1 \text{ MeV}) \gtrsim 0.25[\Gamma/(1 + z)]^2$. The optical depth $\tau_{\gamma\gamma}$ is estimated depending on the relative location between E_{td} and the Band-function break energy. If energy E_{td} lies in between $E_p(\alpha - \beta)/(2 + \alpha)$ and E_c, the general expression for the optical depth is given as,

$$\tau_{\gamma\gamma}(E) = \frac{C(\beta)\sigma_T d_z^2 f_0}{-1 - \beta} \left(\frac{E}{m_e^2 c^4}\right)^{-1-\beta} \frac{1}{R_\gamma^2} \left(\frac{\Gamma}{1 + z}\right)^{2+2\beta},$$

where, the parameters are as defined in Zhang & Pe'er (2009). The above equation includes bulk *Lorentz* factor and gamma ray emission (R_γ) radius as two independent parameters Gupta & Zhang (2008). Therefore, we constrain the $R_\gamma - \Gamma$ diagram for the epochs 2 - 3 s and 3 - 4 s. The best constraints are obtained for the later because of the better constrains on spectral parameters. These are shown by blue and red lines and the shaded region color coded as in Figure 4. The vertical dashed lines are the respective Γs obtained earlier for each epoch, and the black dashed line is the $\Gamma_{0,ext}$ obtained from the blast-wave deceleration (Fraija et al.
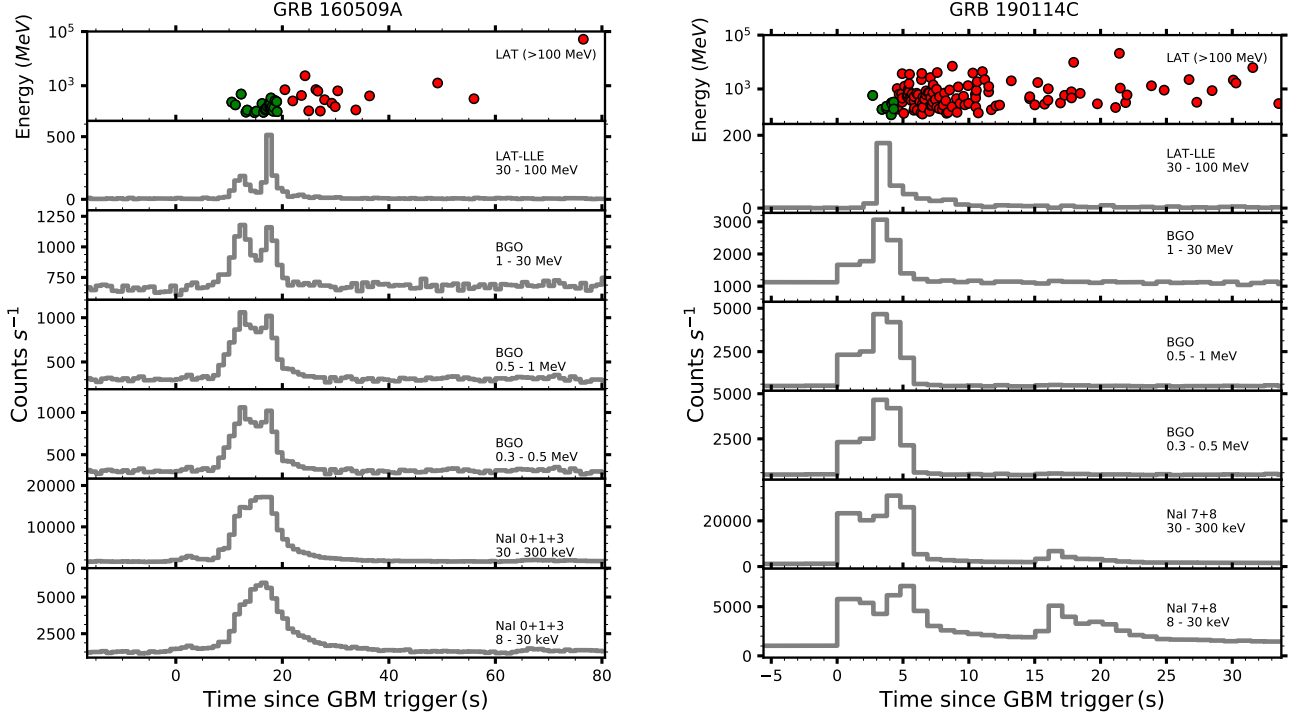
Figure 1. Light-curve evolution of GRB 160509A and GRB 190114C . In the case of GRB 160509A the green filled circles are photons observed before 20 s, and 4.5 s in the case of GRB 190114C with $> 90\%$ probability of their association with the GRBs respectively. Similarly, red filled circles are after these times and with $> 90\%$ probability of their association with the GRB.

Table 1. GRB 190114C : parameters of Band model and Band plus an additional cutoff power-law.

Time	Model	α	β	E_p	K_C	ξ[a]	E_c	Norm	pgstat	AIC	BIC
(s)				(keV)			(MeV)		(dof)		
0-1	B	$-0.66^{+0.02}_{-0.02}$	$-3.08^{+0.16}_{-0.22}$	443^{+16}_{-15}	$0.53^{+0.01}_{-0.01}$	$\cdots$	$\cdots$	$\cdots$	773.14(690)	793.1	838.6
1-2	B	$-0.64^{+0.01}_{-0.01}$	$-3.94^{+0.32}_{-0.64}$	582^{+13}_{-13}	$0.76^{+0.01}_{-0.01}$	$\cdots$	$\cdots$	$\cdots$	796.17(690)	816.1	861.7
2-3	B	$-0.60^{+0.01}_{-0.01}$	$-3.46^{+0.14}_{-0.17}$	743^{+10}_{-17}	$0.52^{+0.01}_{-0.01}$	$\cdots$	$\cdots$	$\cdots$	908.11(692)	928.1	973.6
	B+CPL	$-0.49^{+0.04}_{-0.03}$	$-4.37^{+0.49}_{-4.37}$	720^{+9}_{-18}	$0.49^{+0.01}_{-0.01}$	$1.66^{+0.07}_{-0.1}$	33^{+47}_{-13}	46^{+16}_{-16}	856.45(689)	882.4	941.6
3-4	B	$-0.26^{+0.02}_{-0.01}$	$-2.64^{+0.03}_{-0.03}$	854^{+16}_{-16}	$0.57^{+0.01}_{-0.01}$	$\cdots$	$\cdots$	$\cdots$	1183.8(692)	1203.8	1249.3
	B+CPL	$-0.01^{+0.04}_{-0.04}$	$-3.42^{+0.18}_{-0.22}$	811^{+16}_{-15}	$0.48^{+0.01}_{-0.01}$	$1.37^{+0.03}_{-0.03}$	50^{+10}_{-8}	29^{+5}_{-5}	856.02(689)	882.0	941.2
4-5	B	$-0.46^{+0.01}_{-0.01}$	$-2.88^{+0.05}_{-0.05}$	540^{+10}_{-10}	$0.91^{+0.01}_{-0.01}$	$\cdots$	$\cdots$	$\cdots$	1490.67(692)	1510.7	1556.2
	B+CPL	$-0.12^{+0.03}_{-0.03}$	$-4.03^{+0.32}_{-0.64}$	510^{+9}_{-9}	$0.83^{+0.02}_{-0.02}$	$1.76^{+0.03}_{-0.05}$	474^{+428}_{-177}	198^{+23}_{-27}	850.88(689)	876.9	936.2
5-6	B	$-0.73^{+0.02}_{-0.02}$	$-2.75^{+0.06}_{-0.06}$	450^{+13}_{-13}	$0.64^{+0.01}_{-0.01}$	$\cdots$	$\cdots$	$\cdots$	1066.99(692)	1087.0	1132.5
	B+CPL	$-0.36^{+0.05}_{-0.05}$	$-10.00^{10.00}_{-\infty}$	420^{+11}_{-10}	$0.60^{+0.02}_{-0.01}$	$1.80^{+0.04}_{-0.04}$	183^{+212}_{-71}	225^{+41}_{-38}	715.85(689)	741.8	801.1
6-7	B	$-1.32^{+0.29}_{-0.21}$	$-1.94^{+0.03}_{-0.03}$	54^{+26}_{-14}	$0.18^{+0.2}_{-0.07}$	$\cdots$	$\cdots$	$\cdots$	713.30(692)	733.3	778.8

2019). The $R_\gamma - \Gamma$ beyond the shaded regions is allowed from the observed spectrum with sub-GeV cutoffs.

The time-resolved spectrum also shows a transition from nonthermal to quasi-thermal. A blackbody added to the Band function is the preferred model just after the beginning point of the second pulse, $i.e.$, ~ 2.5 s after the GBM trigger. The spectral slopes are plotted in Figure 5, where the vertical dashed line marks the beginning of the second pulse (t = 2.7 s). At the photosphere, the Γ of the GRB outflow is found from the calculation as given in the (Pe'er et al. 2007).

$$\Gamma_{ph} = \left[(1.06) \left(1 + z\right)^2 d_{\rm L} \frac{Y F_{\gamma,{\rm ob}} \sigma_{\rm T}}{2 m_{\rm p} c^3 \mathcal{R}} \right]^{1/4},$$

where observed energy flux is $F_{\gamma,{\rm ob}}$, Y is the ratio of the total burst energy to the energy emitted in γ-rays
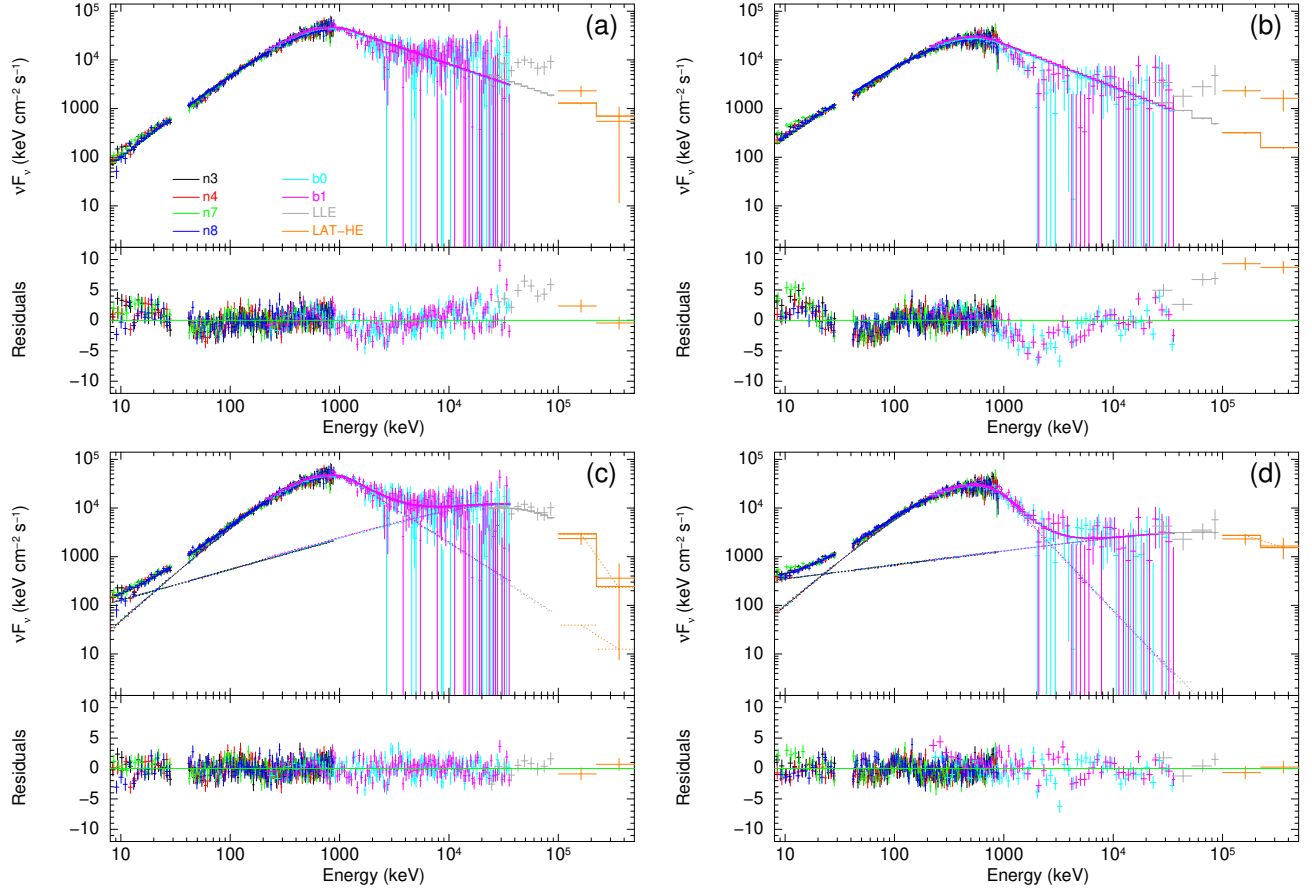
Figure 2. GRB 190114C: *(a)* the unfolded Band model for the $3 - 4\ s$ interval, *(b)* the unfolded Band model fitted for the 4 - 5 s interval, *(c)* the unfolded Band + cutoff power law for the 3 - 4 s interval. *(d)* the unfolded Band + cutoff power law for the 4 - 5 s interval. The lower panel in each plot shows the residuals. A trend can be seen in the residuals when fit with only the Band function.

Table 2. Summary of Γs (Lithwick & Sari 2001)

Lorentz factor Γ	2 - 3 s	3 - 4 s	4 - 5 s
$\Gamma_i = \hat{\tau}^{1/(-2\beta+2)}\left(E_c/m_ec^2\right)^{(-\beta-1)/(-2\beta+2)}(1+z)^{(-\beta-1)/(-\beta+1)}$, where, $\hat{\tau} = \left(2.1\times10^{11}\right)\left[\frac{(d_L/7\ Gpc)^2(0.511)^{\beta+1}f_1}{(\delta T/0.1\ s)(-\beta-1)}\right]$,	115	211	318
$\Gamma_{ii} \approx \frac{E_{cut}}{m_ec^2}(1+z)$	92	139	<u>1317</u>
$\Gamma_{iii} > \hat{\tau}^{1/(-\beta+3)}(1+z)^{(-\beta-1)/(-\beta+3)}(180/11)^{1/(6-2\beta)}$	<u>154</u>	<u>307</u>	210
$E_{\rm syn,max} = \frac{9\Gamma}{4\alpha_F(1+z)}m_ec^2$ in GeV	6.4	15.1	17.7

Here, d_L is the luminosity distance of the burst, β is the Band high-energy index, z is the redshift, δT is the variability timescale, f_1 is photon spectrum (*photon* $s^{-1}\ cm^{-2}\ MeV^{-1}$) at the energy of 1 MeV , and E_c is the cutoff energy. We extract δT from the data by creating Bayesian blocks from the light curves by the relation $\delta T = 2t_{bb}$, t_{bb} is the minimum Bayesian block and α_F is the fine structure constant.

and $\mathcal{R}$ is defined as $\mathcal{R} \equiv \left(\frac{F_{\rm bb,ob}}{\sigma T_{\rm ob}^4}\right)^{1/2}$, such that $F_{\rm bb,ob}$ and $T_{\rm ob}$ are the observed flux and temperature of the blackbody component, respectively. The relevant radii, the initial fireball radius (r_0), the saturation radius (r_s) and the photospheric radius (r_{ph}) are defined in Pe'er et al. 2007. The efficiency for GRB 190114C is taken from Fraija et al. (2019) for calculating the Lorentz fac-

tor ($Y = 6.65$ corresponding to 15% efficiency). The Γs thus determined are reported in Table 3 and are also shown by open circles in Figure 4 with colors representing the epochs.

The hard spectrum during the second pulse may suggest dissipation below the photosphere. The outgoing photons produced in this dissipation undergo process
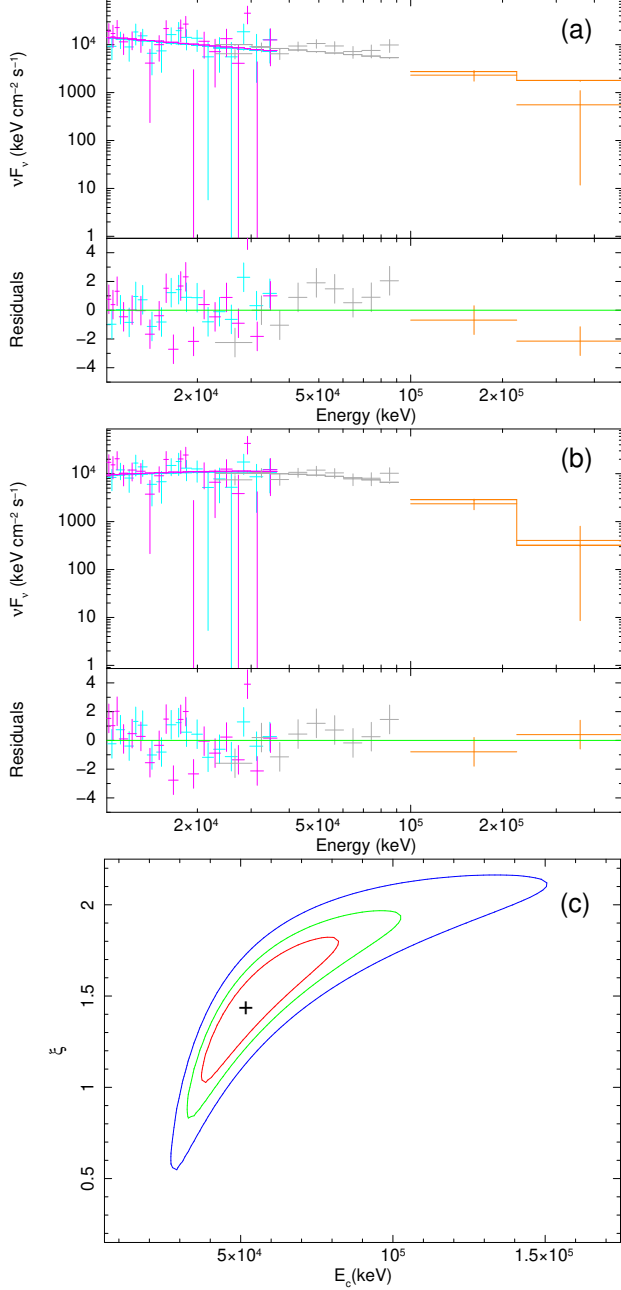
Figure 3. (a) The unfolded power-law fit for energy bands above 10 MeV for the 3 - 4 s interval, (b) same as the top panel but cutoff power-law fit, and (c) confidence intervals (68%, 90%, and 99%) for cutoff energy and power-law index.

Comptonization and escape at the photosphere, which is a fuzzy (*i.e.*, extended) zone (Beloborodov & Mészáros 2017). The specialty of such a model spectrum is its strikingly similar shape as the observed one during this time, and it can account for both the hardness as well as the high-energy cutoff seen in the spectrum. In this scenario, the radiation is emitted at the photospheric radius r_{ph}. The Γ thus obtained is similar to the Γ_{ph},
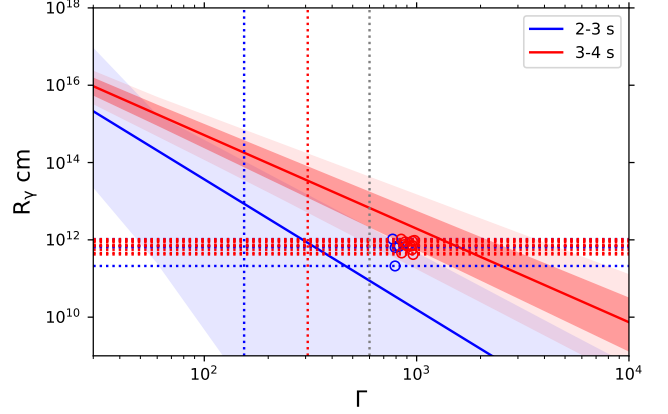
Figure 4. $R_\gamma - \Gamma$ diagram for GRB 190114C are shown for the labeled epochs in blue and red lines, chronologically. The allowed region lies beyond these lines. The points from the photospheric model are also shown in open circles and in the the same color same color convention. Horizontal dashed lines are used here to mark the r_{ph} values. The shaded bands represent the uncertainty in the $R_\gamma - \Gamma$ region obtained by sampling the R_γ from the observed spectral parameters taken in a range within their uncertainties. For the epoch of 3 - 4 s, the sampling is also performed in an interval that is twice the errorbars and shown in a lightened red shade.
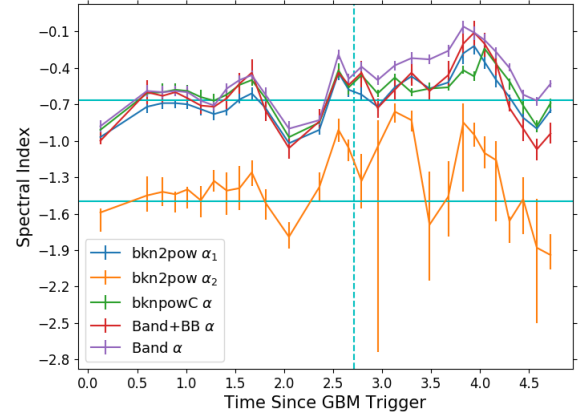
Figure 5. Spectral index evolution for different models.

and within possible uncertainties in the $\Gamma_{0,ext}$. A consistent picture is thus obtained where the prompt emission spectrum showing a sub-GeV cutoff is arising from a subphotospheric zone.

5. DISCUSSION

In the literature, several bright GRBs have shown a peculiar cutoff in the sub-GeV energies (Tang et al. 2015; Wang et al. 2017; Vianello et al. 2017). These GRBs are observed in a broadband. The analysis of

the prompt emission for many GRBs could be marred by limited band observations and also by contamination from the bright afterglow component existing simultaneously with prompt emission. We have shown this here in the case of GRB 190114C (also seen in Ravasio et al. 2019b), and in the case of GRB 160509A , we highlighted the transition region by showing the evolution of prompt emission and afterglows. In the case of GRB 160509A , the effect is feeble while GRB 190114C is severely affected. In our analysis of the joint data from *Fermi* detectors, we have recovered such a break in the time-resolved analysis that could be smeared in the time-integrated emission and at a certain point by the dominating external component.

GRB 190114C also shows a spectacular evolution of the spectral shape. Some bursts with well-separated phases have shown a transition from a fireball dominant outflow to a Poynting flux dominated outflow (Zhang et al. 2018; Li 2019b). Some bursts show a hybrid of thermal and nonthermal components e.g., GRB 100724B, GRB 110721A, and GRB 120323A (Axelsson et al. 2012). In the case of GRB 190114C, initially the emission is nonthermal and can be a synchrotron emission from internal shock with a weak photospheric component. The initial spectrum becomes hard after ~ 2.5 s where a fresh injection seems to be occurring. Such a hard spectrum can be possible in the case of dissipation occurring at a region below the photosphere, which is

optically thick ($\tau > 1$). By this time the first pulse contribution is also subdominant. The shape of the spectrum can be explained in such a case arising from the Comptonization of the outgoing photons. The observed sub-GeV cutoff in the spectrum helps constrain the site of the prompt emission observed in GRB 190114C . The complete picture from this analysis would be as follows: (a) the initial phase is produced away from the photosphere, (b) the second hard phase is produced in a sub-photospheric dissipation, and (c) the afterglow is produced in the external shock; the sub-TeV radiation is also consistent with this picture arising from inverse-Compton scattering (Fraija et al. 2019; MAGIC Collaboration et al. 2019) in the external shocks.

APPENDIX

A. SPECTRAL MODELS

The Band model is given by:

$$N_{\mathrm{B}}(E) = \begin{cases} K_B(E/100)^{\alpha}\exp\left(-E\left(2+\alpha\right)/E_{\mathrm{p}}\right) & , E < E_{\mathrm{b}} \\ K_B\{(\alpha-\beta)\,E_{\mathrm{p}}/\left[100\left(2+\alpha\right)\right]\}^{(\alpha-\beta)}\exp\left(\beta-\alpha\right)\left(E/100\right)^{\beta} & , E \geq E_{\mathrm{b}} \end{cases}, \tag{A1}$$

where $E_b = (\alpha-\beta)E_p/(2+\alpha)$. The Band model with a high-energy exponential cutoff at E_c (BC) is given by

$$N_{\mathrm{BC}}(E) = N_{\mathrm{B}}(E) \times exp\left(-\frac{E}{E_c}\right). \tag{A2}$$

Other models considered in this paper include a `blackbody`[4] (BB), blackbody added to Band (B+BB), a broken power-law model with two breaks (`bkn2pow`[5]), a broken power-law model with one break and a high-energy cutoff (`bknpowC`[6]), and a power-law model with a high-energy exponential cutoff added to `blackbody` (BB+CPL[7]), as given by:

$$N_{B+BB}(E) = N_B(E) + K_{BB}\frac{E^2}{exp(E/kT_{BB})-1} \tag{A3}$$

[4] https://heasarc.gsfc.nasa.gov/xanadu/xspec/manual/node137.html
[5] https://heasarc.gsfc.nasa.gov/xanadu/xspec/manual/node141.html
[6] https://heasarc.gsfc.nasa.gov/xanadu/xspec/manual/node142.html
[7] https://heasarc.gsfc.nasa.gov/xanadu/xspec/manual/node160.html

Table 3. Time-resolved Spectral fitting for different models

B Sr. no.	(t_1, t_2)	α	β	$E_p\ (keV)$	K_B	AIC	BIC	BIC model (B, BB + B)	AIC model preferred model
								$dof = 560$	
1	$(-0.26,\ 0.51)$	$-0.88^{+0.05}_{-0.05}$	$-2.84^{+0.34}_{-1.34}$	466^{+60}_{-53}	$0.16^{+0.01}_{-0.01}$	693.0	727.8	B	bknpowC, BB + CPL, bkn2pow, BB + B, B
2	$(0.51,\ 0.69)$	$-0.59^{+0.05}_{-0.05}$	$-3.0^{+0.3}_{-0.5}$	417^{+31}_{-30}	$0.71^{+0.05}_{-0.04}$	556.0	590.7	B	B, bkn2pow, BB + B, bknpowC
3	$(0.69,\ 0.83)$	$-0.60^{+0.05}_{-0.05}$	$-2.9^{+0.2}_{-0.4}$	439^{+34}_{-32}	$0.86^{+0.06}_{-0.05}$	559.1	593.8	B, BB + B	bkn2pow, BB + B, B
4	$(0.83,\ 0.95)$	$-0.59^{+0.04}_{-0.04}$	$-3.8^{+0.6}_{-\infty}$	465^{+28}_{-27}	$0.95^{+0.05}_{-0.05}$	510.9	545.6	B	bknpowC, BB + CPL, BB + B, B, bkn2pow
5	$(0.95,\ 1.08)$	$-0.60^{+0.05}_{-0.05}$	$-3.36^{+0.42}_{-1.15}$	423^{+29}_{-27}	$0.97^{+0.06}_{-0.05}$	564.0	598.7	B	bknpowC, BB + B, BB + CPL, B
6	$(1.08,\ 1.22)$	$-0.67^{+0.04}_{-0.04}$	$-3.5^{+0.4}_{-2.8}$	504^{+36}_{-35}	$0.84^{+0.05}_{-0.04}$	507.7	542.5	B, BB + B	bknpowC, BB + CPL, BB + B
7	$(1.22,\ 1.35)$	$-0.71^{+0.04}_{-0.03}$	$-9.4^{+5.1}_{-\infty}$	656^{+40}_{-38}	$0.74^{+0.03}_{-0.03}$	514.8	549.6	B	bknpowC, B, BB + CPL, bkn2pow, BB + B
8	$(1.35,\ 1.48)$	$-0.57^{+0.04}_{-0.04}$	$-4^{+0.5}_{-3.4}$	645^{+34}_{-32}	$0.84^{+0.04}_{-0.03}$	569.1	603.8	B , BB + B	BB + B, bkn2pow, BB + CPL, bknpowC, B
9	$(1.48,\ 1.61)$	$-0.50^{+0.04}_{-0.04}$	$-4.1^{+0.6}_{-\infty}$	593^{+31}_{-29}	$0.89^{+0.04}_{-0.04}$	473.3	508.1	B	B, bknpowC, BB + B, BB + CPL
10	$(1.61,\ 1.73)$	$-0.46^{+0.04}_{-0.04}$	$-5.6^{+4.1}_{-\infty}$	727^{+33}_{-32}	$0.88^{+0.04}_{-0.04}$	602.9	637.6	B	B, bknpowC, BB + CPL, BB + B
11	$(1.73,\ 1.89)$	$-0.62^{+0.06}_{-0.06}$	$-2.70^{+0.18}_{-0.31}$	346^{+36}_{-32}	$0.84^{+0.08}_{-0.07}$	577.3	612.0	BB + B, B	bknpowC, BB + B, BB + CPL, bkn2pow
12	$(1.89,\ 2.21)$	$-0.90^{+0.07}_{-0.06}$	$-2.58^{+0.23}_{-0.53}$	317^{+51}_{-43}	$0.37^{+0.05}_{-0.03}$	580.8	615.5	B, BB + B	bknpowC, BB + CPL, bkn2pow, BB + B
13	$(2.21,\ 2.51)$	$-0.83^{+0.04}_{-0.04}$	$-9.4^{+0.9}_{-\infty}$	676^{+56}_{-74}	$0.34^{+0.02}_{-0.02}$	545.2	579.9	B	bkn2pow, B, bknpowC, BB + CPL, BB + B
14	$(2.51,\ 2.60)$	$-0.29^{+0.04}_{-0.04}$	$-4.3^{+0.6}_{-\infty}$	742^{+32}_{-30}	$1.16^{+0.05}_{-0.05}$	552.6	587.4	B	bkn2pow, B, bknpowC, BB + CPL, BB + B
15	$(2.60,\ 2.72)$	$-0.49^{+0.04}_{-0.04}$	$-3.6^{+0.3}_{-0.6}$	763^{+40}_{-36}	$0.81^{+0.03}_{-0.03}$	628.5	663.2	B	bkn2pow, B
16	$(2.72,\ 2.86)$	$-0.39^{+0.04}_{-0.04}$	$-4.9^{+1.1}_{-\infty}$	678^{+31}_{-27}	$0.72^{+0.03}_{-0.03}$	568.6	603.4	B, BB + B	bknpowC, BB + B, BB + CPL
17	$(2.86,\ 3.05)$	$-0.50^{+0.04}_{-0.04}$	$-3.4^{+0.3}_{-0.4}$	823^{+44}_{-41}	$0.51^{+0.02}_{-0.02}$	628.5	663.2	BB + B	BB + B, bkn2pow
18	$(3.05,\ 3.21)$	$-0.38^{+0.04}_{-0.04}$	$-2.66^{+0.10}_{-0.11}$	963^{+52}_{-49}	$0.54^{+0.02}_{-0.02}$	696.1	730.9	BB + B	BB + B, bkn2pow
19	$(3.21,\ 3.39)$	$-0.32^{+0.05}_{-0.05}$	$-2.47^{+0.08}_{-0.09}$	835^{+48}_{-45}	$0.51^{+0.02}_{-0.02}$	613.6	648.3	BB + B	BB + B
20	$(3.39,\ 3.58)$	$-0.33^{+0.04}_{-0.04}$	$-3.24^{+0.20}_{-0.27}$	939^{+40}_{-41}	$0.51^{+0.02}_{-0.02}$	646.8	681.5	BB + B	BB + B
21	$(3.58,\ 3.77)$	$-0.26^{+0.05}_{-0.05}$	$-2.93^{+0.14}_{-0.17}$	877^{+41}_{-40}	$0.46^{+0.02}_{-0.02}$	731.6	766.3	BB + B	BB + B
22	$(3.77,\ 3.89)$	$-0.06^{+0.06}_{-0.05}$	$-2.69^{+0.09}_{-0.11}$	815^{+39}_{-37}	$0.72^{+0.03}_{-0.03}$	660.3	695.0	BB + B	BB + B
23	$(3.89,\ 3.99)$	$-0.11^{+0.06}_{-0.05}$	$-2.66^{+0.10}_{-0.11}$	690^{+35}_{-34}	$0.98^{+0.05}_{-0.04}$	661.8	696.6	B , BB + B	bkn2pow
24	$(3.99,\ 4.10)$	$-0.17^{+0.05}_{-0.05}$	$-3.5^{+0.3}_{-0.4}$	668^{+29}_{-27}	$0.97^{+0.04}_{-0.04}$	643.4	678.2	B	bkn2pow, BB + B
25	$(4.10,\ 4.23)$	$-0.27^{+0.05}_{-0.04}$	$-3.37^{+0.27}_{-0.42}$	607^{+27}_{-28}	$0.88^{+0.04}_{-0.04}$	641.7	676.4	BB + B	BB + B
26	$(4.23,\ 4.37)$	$-0.40^{+0.03}_{-0.04}$	$-3.29^{+0.26}_{-0.41}$	412^{+7}_{-21}	$1.03^{+0.02}_{-0.05}$	581.5	616.3	BB + B	bkn2pow, BB + B
27	$(4.37,\ 4.51)$	$-0.62^{+0.05}_{-0.04}$	$-3.42^{+0.50}_{-\infty}$	424^{+27}_{-26}	$0.88^{+0.05}_{-0.05}$	627.8	662.6	BB + B	bkn2pow, BB + B, BB + CPL
28	$(4.51,\ 4.65)$	$-0.67^{+0.04}_{-0.03}$	$-4.3^{+0.7}_{-\infty}$	520^{+11}_{-29}	$0.83^{+0.02}_{-0.03}$	653.0	687.7	BB + B	BB + CPL, BB + B
29	$(4.65,\ 4.79)$	$-0.53^{+0.03}_{-0.03}$	$-4.34^{+0.76}_{-\infty}$	615^{+12}_{-12}	$0.77^{+0.01}_{-0.01}$	671.0	705.7	BB + B	BB + CPL, BB + B

$b:\ photons\ keV^{-1}\ cm^{-2}\ s^{-1}$ at 1 keV

$$N_{\text{bkn2pow}}(E) = \begin{cases} K^b E^{-\alpha_1} & ,\ E \leq E_1 \\ K^b E_1^{\alpha_2 - \alpha_1} E^{-\alpha_2} & ,\ E_1 \leq E \leq E_2 \\ K^b E_1^{\alpha_2 - \alpha_1} E_2^{-\beta - \alpha_2} E^{\beta} & ,\ \text{E} \geq \text{E}_3 \end{cases}, \tag{A4}$$

$$N_{\text{bkn2powC}}(E) = N_{\text{bkn2pow}}(E) \times exp\left(-\frac{E}{E_c}\right). \tag{A5}$$

$$N_{\text{bknpow}}(E) = \begin{cases} K E^{-\alpha_1} & ,\ E \leq E_1 \\ K E_1^{\alpha_2 - \alpha_1} (E/1keV)^{-\alpha_2} & ,\ E > E_1 \end{cases} \tag{A6}$$

$$N_{\text{bknpowC}}(E) = N_{\text{bknpow}}(E) \times exp\left(-\frac{E}{E_c}\right). \tag{A7}$$

$$N_{BB+CPL}(E) = K_{BB} \frac{E^2}{exp(E/kT_{BB}) - 1} + K_C E^{-\xi} exp\left(-\frac{E}{E_c}\right) \tag{A8}$$

B. GRB 160509A LAT-HE: SUB-GEV CUTOFF AND TRANSITION FROM PROMPT TO AFTERGLOW

A high-energy cutoff (around 100 MeV) to the Band function is found to be the best-fit model in the case of GRB 160509A . In some other GRBs also, a sub-GeV cutoff is seen (Abdo et al. 2009; Tang et al. 2015; Vianello et al. 2017). LAT emission can be divided into two major episodes (arising due to prompt and afterglow) and these episodes can superimpose. For GRB 160509A , we observe a transition from prompt to afterglows and note some of the properties shown by the emission observed in LAT.

Table 3. Time-resolved Spectral fitting (continued)

B + BB							$dof = 558$					
Sr. no.	(t_1,t_2)	α	β	E_p	K_B	kT_{BB}	K_{BB}	AIC	BIC	Γ_{ph}	r_{ph}	r_s
Sr. no.	in s			(keV)		(keV)				$(Y = 6.65)$	$(10^{11}\ cm)$	$(10^{11}\ cm)$
1	$(-0.26, 0.51)$	$-1.0^{+0.03}_{-0.07}$	$-3.6^{+0.9}_{-\infty}$	609^{+93}_{-91}	$0.12^{+0.03}_{-0.02}$	43^{+6}_{-6}	$9.5^{+5.7}_{-3.4}$	692.0	735.4	$\cdots$	$\cdots$	$\cdots$
2	$(0.51, 0.69)$	$-0.6^{+0.1}_{-0.1}$	$-3.14^{+0.33}_{-0.74}$	449^{+63}_{-78}	$0.63^{+0.11}_{-0.10}$	$40^{+\infty}_{-40}$	19^{+33}_{-19}	558.0	601.4	$\cdots$	$\cdots$	$\cdots$
3	$(0.69, 0.83)$	$-0.63^{+0.07}_{-0.07}$	$-3.1^{+0.3}_{-0.51}$	488^{+52}_{-45}	$0.74^{+0.09}_{-0.08}$	33^{+11}_{-10}	28^{+25}_{-18}	555.3	598.7	$\cdots$	$\cdots$	$\cdots$
4	$(0.83, 0.95)$	$-0.60^{+0.03}_{-0.04}$	$-4.0^{+0.7}_{-\infty}$	490^{+11}_{-23}	$0.86^{+0.02}_{-0.07}$	32^{+8}_{-6}	$23^{+19}_{-6.6}$	509.8	553.3	$\cdots$	$\cdots$	$\cdots$
5	$(0.95, 1.08)$	$-0.65^{+0.03}_{-0.08}$	$-3.65^{+0.50}_{-2.86}$	463^{+11}_{-38}	$0.83^{+0.06}_{-0.11}$	39^{+7}_{-10}	36^{+37}_{-20}	562.6	606.0	$\cdots$	$\cdots$	$\cdots$
6	$(1.08, 1.22)$	$-0.71^{+0.07}_{-0.07}$	$-3.9^{+0.8}_{-\infty}$	559^{+61}_{-52}	$0.72^{+0.08}_{-0.08}$	36^{+11}_{-12}	34^{+29}_{-22}	502.5	545.9	$\cdots$	$\cdots$	$\cdots$
7	$(1.22, 1.35)$	$-0.72^{+0.03}_{-0.04}$	$-10^{+10}_{-\infty}$	671^{+25}_{-17}	$0.71^{+0.16}_{-0.05}$	$35^{+\infty}_{-35}$	12^{+19}_{-12}	517.0	560.6	$\cdots$	$\cdots$	$\cdots$
8	$(1.35, 1.48)$	$-0.65^{+0.09}_{-0.08}$	$-3.7^{+0.9}_{-1.9}$	620^{+84}_{-233}	$0.76^{+0.11}_{-0.08}$	158^{+49}_{-38}	216^{+337}_{-122}	564.2	607.6	$\cdots$	$\cdots$	$\cdots$
9	$(1.48, 1.61)$	$-0.53^{+0.08}_{-0.09}$	$-3.8^{+0.9}_{-4.5}$	574^{+76}_{-214}	$0.86^{+0.13}_{-0.10}$	160^{+129}_{-92}	104^{+398}_{-104}	475.8	519.2	$\cdots$	$\cdots$	$\cdots$
10	$(1.61, 1.73)$	$-0.44^{+0.08}_{-0.11}$	$-3.5^{+0.7}_{-\infty}$	495^{+246}_{-130}	$0.94^{+0.17}_{-0.14}$	239^{+760}_{-239}	608^{+259}_{-608}	604.9	648.3	$\cdots$	$\cdots$	$\cdots$
11	$(1.73, 1.89)$	$-0.75^{+0.09}_{-0.09}$	$-3.15^{+0.41}_{-\infty}$	451^{+63}_{-58}	$0.60^{+0.10}_{-0.08}$	$33^{+6.5}_{-7.1}$	41^{+23}_{-20}	567.7	611.1	$\cdots$	$\cdots$	$\cdots$
12	$(1.89, 2.21)$	$-1.06^{+0.09}_{-0.08}$	$-3.2^{+0.6}_{-\infty}$	455^{+91}_{-77}	$0.26^{+0.05}_{-0.04}$	32^{+6}_{-7}	18^{+9}_{-9}	574.2	617.6	$\cdots$	$\cdots$	$\cdots$
13	$(2.21, 2.51)$	$-0.84^{+0.07}_{-0.10}$	$-3.73^{+0.98}_{-\infty}$	654^{+161}_{-252}	$0.33^{+0.04}_{-0.05}$	$156^{+\infty}_{-124}$	23^{+128}_{-23}	547.9	591.4	$\cdots$	$\cdots$	$\cdots$
14	$(2.51, 2.60)$	$-0.44^{+0.03}_{-0.03}$	$-10.0^{+10.0}_{-\infty}$	797^{+17}_{-17}	$0.97^{+0.02}_{-0.02}$	153^{+11}_{-10}	455^{+41}_{-40}	550.4	593.8	846	12.0	0.98
15	$(2.60, 2.72)$	$-0.54^{+0.03}_{-0.03}$	$-10^{+10}_{-\infty}$	758^{+17}_{-17}	$0.77^{+0.01}_{-0.01}$	201^{+32}_{-27}	169^{+33}_{-33}	641.2	684.7	962	11.6	0.91
16	$(2.72, 2.86)$	$-0.44^{+0.12}_{-0.10}$	$-3.1^{+0.6}_{-3.6}$	466^{+229}_{-173}	$0.71^{+0.15}_{-0.10}$	195^{+23}_{-45}	536^{+252}_{-374}	562.3	605.7	828	11.8	1.00
17	$(2.86, 3.05)$	$-0.73^{+0.08}_{-0.08}$	$-2.67^{+0.38}_{-0.40}$	735^{+191}_{-277}	$0.40^{+0.05}_{-0.04}$	184^{+19}_{-19}	448^{+183}_{-106}	575.2	618.6	808	11.8	0.99
18	$(3.05, 3.21)$	$-0.58^{+0.08}_{-0.08}$	$-2.30^{+0.18}_{-0.15}$	929^{+8849}_{-214}	$0.44^{+0.04}_{-0.04}$	208^{+23}_{-18}	573^{+184}_{-146}	657.0	700.4	954	11.8	0.98
19	$(3.21, 3.39)$	$-0.44^{+0.11}_{-0.08}$	$-2.06^{+0.17}_{-0.16}$	621^{+177}_{-199}	$0.46^{+0.07}_{-0.04}$	205^{+16}_{-19}	524^{+178}_{-165}	585.0	628.4	935	11.8	0.97
20	$(3.39, 3.58)$	$-0.59^{+0.07}_{-0.03}$	$-2.78^{+0.22}_{-0.20}$	1000^{+8937}_{-143}	$0.39^{+0.03}_{-0.01}$	192^{+19}_{-9}	546^{+126}_{-29}	607.3	650.7	875	11.8	0.99
21	$(3.58, 3.77)$	$-0.46^{+0.09}_{-0.12}$	$-2.22^{+0.16}_{-0.33}$	616^{+358}_{-138}	$0.39^{+0.04}_{-0.06}$	212^{+13}_{-30}	682^{+131}_{-213}	690.2	733.6	899	11.8	1.00
22	$(3.77, 3.89)$	$-0.2^{+0.1}_{-0.1}$	$-2.14^{+0.14}_{-0.17}$	584^{+146}_{-111}	$0.64^{+0.07}_{-0.07}$	211^{+14}_{-14}	1054^{+216}_{-272}	632.3	675.7	977	11.9	1.00
23	$(3.89, 3.99)$	$-0.11^{+0.13}_{-0.10}$	$-2.25^{+0.17}_{-0.24}$	479^{+146}_{-116}	$1.00^{+0.17}_{-0.11}$	200^{+22}_{-14}	822^{+274}_{-428}	655.7	699.1	954	11.9	0.99
24	$(3.99, 4.10)$	$-0.20^{+0.11}_{-0.09}$	$-2.7^{+0.3}_{-0.6}$	475^{+201}_{-124}	$0.96^{+0.14}_{-0.11}$	194^{+25}_{-43}	774^{+299}_{-565}	641.2	684.7	883	11.9	1.01
25	$(4.10, 4.23)$	$-0.36^{+0.10}_{-0.10}$	$-2.43^{+0.19}_{-0.29}$	381^{+113}_{-77}	$0.83^{+0.11}_{-0.10}$	161^{+12}_{-9}	675^{+134}_{-198}	625.6	669.0	771	12.0	1.02
26	$(4.23, 4.37)$	$-0.73^{+0.03}_{-0.10}$	$-3.05^{+0.27}_{-0.52}$	524^{+17}_{-58}	$0.60^{+0.07}_{-0.09}$	74^{+4}_{-7}	212^{+13}_{-60}	563.1	606.6	507	12.2	1.01
27	$(4.37, 4.51)$	$-0.9^{+0.1}_{-0.1}$	$-2.83^{+0.31}_{-0.65}$	511^{+87}_{-83}	$0.56^{+0.11}_{-0.09}$	$75^{+13.1}_{-8.2}$	170^{+48}_{-51}	607.7	651.1	507	12.2	1.00
28	$(4.51, 4.65)$	$-1.07^{+0.09}_{-0.09}$	$-3.6^{+0.8}_{-\infty}$	621^{+134}_{-106}	$0.47^{+0.07}_{-0.06}$	$105^{+8.8}_{-7.4}$	356^{+58}_{-56}	567.0	610.4	582	12.1	1.03
29	$(4.65, 4.79)$	$-0.94^{+0.08}_{-0.09}$	$-3.73^{+0.73}_{-\infty}$	837^{+139}_{-105}	$0.44^{+0.06}_{-0.05}$	114^{+8}_{-7}	416^{+76}_{-61}	603.9	647.3	628	12.1	1.02

b: $photons\ keV^{-1}\ cm^{-2}\ s^{-1}$ at 1 keV

1. Initially, the emission is observed simultaneously with GBM. The LAT-HE flux evolution shows two components with different hardness (see the left panel of Fig. 6), the former being a softer emission that lasts until $\sim 40s$ and the latter being a harder extended emission. The former is a fast varying (FV) component since its photon flux varies with time as $\propto t^{-3.98\pm0.53}$, the latter being a slow varying (SV) LAT-HE component that may extend to an earlier time, thus showing us hardening of the spectral component as a result of its superposition with the earlier softer emission.

2. We, here, track the hard component by monitoring the LAT emission during the overlapping time-window, which helps us smoothly observe the evolution of the spectral index. The FV component is soft and in the time-integrated spectrum can be thought to be the spectrum above the cutoff in the Band spectrum. The two components are dominant in different energy regions. The FV component is majorly populated by the photons with energies that are less than 200 MeV whereas the SV component by ones with energy greater than 200 MeV. The light curves in Fig. 1 (right panel) show photons with energies near 1 GeV that are first observed after $\sim 20\ s$. This implies the presence of LAT-HE afterglow starting earlier than or beginning from 20 s. This claim can further be supported by the flux evolution of LAT in the energy range 0.1-10 GeV as seen in Fig. 6.

3. By looking at the evolution of spectral index, we clearly see the transition from prompt to afterglow emission. In wider bins, this soft to hard transition can be seen in the 20 - 27 s and 27 - 37 s bins. To see this as a smooth transition we made narrower bins of 3 s duration and used the sliding window technique with a step of 1 s, or 2 s (for the last few bins). We plot the spectral index of the power-law fit obtained for these windows. The index evolves from a softer value observed in the bins 8 - 13, 13 - 15, and 15 - 18 s to a harder value observed for the bins after 37 s (see Fig 6).

Table 3. Time-resolved Spectral fitting (continued)

BB+CPL								$dof = 559$
Sr. no.	(t_1, t_2)	ξ	E_c	K_C	kT_{BB}	K_{BB}	AIC	BIC
1	$(-0.26, 0.51)$	$1.00^{+0.08}_{-0.08}$	619^{+199}_{-132}	$12.49^{+3.62}_{-2.80}$	43^{+10}_{-10}	9^{+6}_{-6}	690.5	729.6
2	$(0.51, 0.69)$	$0.70^{+0.07}_{-0.09}$	381^{+28}_{-29}	$13.81^{+3.17}_{-3.47}$	45^{+7}_{-4}	36^{+24}_{-6}	562.0	601.1
3	$(0.69, 0.83)$	$0.66^{+0.07}_{-0.06}$	393^{+58}_{-43}	$15.09^{+4.31}_{-3.37}$	35^{+10}_{-9}	37^{+26}_{-19}	563.1	602.2
4	$(0.83, 0.95)$	$0.60^{+0.04}_{-0.07}$	355^{+22}_{-19}	$14.12^{+2.28}_{-3.36}$	32^{+8}_{-6}	24^{+20}_{-7}	509.8	548.9
5	$(0.95, 1.08)$	$0.67^{+0.08}_{-0.07}$	359^{+53}_{-36}	$17.73^{+5.25}_{-3.74}$	40^{+8}_{-9}	42^{+38}_{-20}	563.0	602.1
6	$(1.08, 1.22)$	$0.73^{+0.06}_{-0.06}$	446^{+63}_{-49}	$19.51^{+5.02}_{-4.25}$	36^{+10}_{-11}	38^{+27}_{-21}	501.1	540.2
7	$(1.22, 1.35)$	$0.72^{+0.04}_{-0.04}$	523^{+52}_{-42}	$19.45^{+3.65}_{-3.28}$	$34^{+\infty}_{-18}$	11^{+19}_{-12}	515.1	554.2
8	$(1.35, 1.48)$	$0.66^{+0.08}_{-0.08}$	479^{+84}_{-99}	$15.80^{+5.11}_{-3.76}$	150^{+55}_{-34}	199^{+145}_{-112}	565.6	604.7
9	$(1.48, 1.61)$	$0.55^{+0.09}_{-0.08}$	419^{+68}_{-86}	$10.49^{+3.77}_{-2.70}$	$125^{+\infty}_{-125}$	77^{+160}_{-77}	476.5	515.6
10	$(1.61, 1.73)$	$0.48^{+0.07}_{-0.09}$	442^{+78}_{-162}	$7.96^{+2.47}_{-2.03}$	242^{+223}_{-129}	198^{+545}_{-198}	603.4	642.5
11	$(1.73, 1.89)$	$0.77^{+0.07}_{-0.07}$	390^{+65}_{-50}	$20.09^{+5.78}_{-4.56}$	34^{+6}_{-6}	45^{+21}_{-18}	567.9	607.0
12	$(1.89, 2.21)$	$1.07^{+0.08}_{-0.08}$	505^{+145}_{-98}	$35.6^{+9.79}_{-7.79}$	32^{+6}_{-7}	18^{+9}_{-9}	573.0	612.1
13	$(2.21, 2.51)$	$0.86^{+0.08}_{-0.07}$	631^{+134}_{-148}	$16.81^{+5.00}_{-3.78}$	$65^{+\infty}_{-33}$	13^{+53}_{-13}	546.1	585.2
14	$(2.51, 2.60)$	$0.44^{+0.09}_{-0.09}$	512^{+75}_{-59}	$7.49^{+2.95}_{-2.15}$	152^{+29}_{-20}	455^{+225}_{-240}	548.4	587.5
15	$(2.60, 2.72)$	$0.54^{+0.07}_{-0.05}$	520^{+65}_{-86}	$9.21^{+2.65}_{-1.91}$	200^{+85}_{-61}	169^{+211}_{-87}	639.3	678.4
16	$(2.72, 2.86)$	$0.48^{+0.09}_{-0.08}$	431^{+67}_{-110}	$6.02^{+2.20}_{-1.57}$	170^{+52}_{-34}	239^{+236}_{-136}	563.1	602.2
17	$(2.86, 3.05)$	$0.80^{+0.08}_{-0.08}$	808^{+179}_{-135}	$14.17^{+4.71}_{-3.57}$	164^{+14}_{-12}	390^{+80}_{-82}	594.7	633.7
18	$(3.05, 3.21)$	$0.94^{+0.07}_{-0.06}$	2393^{+515}_{-405}	$21.74^{+5.17}_{-4.34}$	172^{+8}_{-8}	817^{+100}_{-100}	741.0	780.1
19	$(3.21, 3.39)$	$0.96^{+0.06}_{-0.06}$	2793^{+831}_{-609}	$19.55^{+5.11}_{-4.33}$	152^{+7}_{-7}	666^{+82}_{-85}	744.3	783.4
20	$(3.39, 3.58)$	$0.71^{+0.08}_{-0.08}$	1038^{+207}_{-164}	$8.69^{+3.02}_{-2.34}$	171^{+11}_{-10}	577^{+114}_{-118}	634.7	673.8
21	$(3.58, 3.77)$	$0.76^{+0.09}_{-0.09}$	1365^{+384}_{-284}	$9.69^{+3.71}_{-2.81}$	163^{+8}_{-8}	615^{+104}_{-106}	764.2	803.3
22	$(3.77, 3.89)$	$0.84^{+0.07}_{-0.08}$	2161^{+566}_{-456}	$13.42^{+4.24}_{-3.55}$	158^{+6}_{-7}	1278^{+142}_{-152}	758.1	797.2
23	$(3.89, 3.99)$	$0.70^{+0.10}_{-0.13}$	1188^{+400}_{-315}	$11.06^{+4.99}_{-4.06}$	123^{+7}_{-9}	858^{+179}_{-214}	808.6	847.7
24	$(3.99, 4.10)$	$0.32^{+0.11}_{-0.12}$	444^{+77}_{-115}	$3.45^{+1.73}_{-1.19}$	121^{+41}_{-45}	244^{+202}_{-215}	658.9	698.0
25	$(4.10, 4.23)$	$0.46^{+0.10}_{-0.11}$	443^{+80}_{-63}	$5.85^{+2.63}_{-1.85}$	121^{+26}_{-17}	274^{+130}_{-140}	649.0	688.0
26	$(4.23, 4.37)$	$0.73^{+0.09}_{-0.10}$	451^{+52}_{-77}	$19.15^{+6.90}_{-5.49}$	73^{+3}_{-6}	221^{+12}_{-61}	569.5	608.6
27	$(4.37, 4.51)$	$0.86^{+0.09}_{-0.09}$	444^{+100}_{-73}	$31.33^{+11.32}_{-8.45}$	74^{+12}_{-9}	147^{+49}_{-52}	612.2	651.3
28	$(4.51, 4.65)$	$1.07^{+0.08}_{-0.08}$	687^{+190}_{-138}	$65.61^{+20.22}_{-15.73}$	104^{+8}_{-7}	355^{+57}_{-56}	565.2	604.3
29	$(4.65, 4.79)$	$0.95^{+0.01}_{-0.01}$	810^{+44}_{-40}	$34.01^{+0.95}_{-1.23}$	$113^{+4.0}_{-3}$	416^{+18}_{-20}	602.7	641.8

To summarize, sub-GeV spectral cutoffs may not be very evident in the time-integrated spectrum of the prompt emission. However, if the LAT photon index shows soft to hard evolution, this is a first hint of a spectral cutoff at sub-GeV energies. The time-resolved spectra can show a cutoff in the spectral bins where it is actually present. The transition from the prompt to afterglows can be studied by sliding a coarse bin with size which has a well-constrained photon index. The evolution of the photon index would become significant as the external component will start shaping the spectrum. The start point can also be marked by observing the photon light curve in an unbinned likelihood analysis of the LAT data.

VIKAS CHAND ET AL.

Table 3. Time-resolved Spectral fitting (continued)

bknpowC							$dof = 559$	
Sr. no.	(t_1,t_2)	α_1	E_1 (keV)	α_2	K	E_c	AIC	BIC
1	$(-0.26\ ,\ 0.51)$	$0.91^{+0.04}_{-0.04}$	$137.17^{+20.83}_{-17.3}$	$1.35^{+0.23}_{-0.23}$	$9.61^{+1.38}_{-1.28}$	$892.85^{+554.67}_{-209.79}$	687.4	726.5
2	$(0.51\ ,\ 0.69)$	$0.61^{+0.03}_{-0.03}$	$129.62^{+10.17}_{-13.24}$	$0.97^{+0.2}_{-0.21}$	$11.02^{+1.42}_{-1.34}$	$447.91^{+101.7}_{-46.01}$	559.8	598.9
3	$(0.69\ ,\ 0.83)$	$0.6^{+0.06}_{-0.07}$	$110.42^{+27.47}_{-30.16}$	$0.96^{+0.19}_{-0.09}$	$12.69^{+3.05}_{-2.81}$	$482.62^{+131.31}_{-85.63}$	561.6	600.7
4	$(0.83\ ,\ 0.95)$	$0.58^{+0.03}_{-0.05}$	$114.67^{+25.36}_{-29.45}$	$0.79^{+0.15}_{-0.1}$	$13.43^{+1.63}_{-1.8}$	$398.66^{+55.02}_{-35.14}$	510.2	549.3
5	$(0.95\ ,\ 1.08)$	$0.59^{+0.05}_{-0.05}$	$114.43^{+35.77}_{-23.51}$	$0.89^{+0.21}_{-0.17}$	$14.53^{+2.82}_{-2.54}$	$406.72^{+91.89}_{-52.53}$	561.8	600.9
6	$(1.08\ ,\ 1.22)$	$0.64^{+0.06}_{-0.06}$	$107.77^{+41.31}_{-61.34}$	$0.95^{+0.19}_{-0.15}$	$16.07^{+3.9}_{-3.2}$	$522.58^{+127.46}_{-81.46}$	500.1	539.2
7	$(1.22\ ,\ 1.35)$	$0.67^{+0.06}_{-0.06}$	$324.51^{+96.88}_{-97.93}$	$0.28^{+0.39}_{-0.43}$	$17.51^{+5.43}_{-3.39}$	$391.94^{+214.55}_{-75.27}$	513.4	552.5
8	$(1.35\ ,\ 1.48)$	$0.62^{+0.03}_{-0.05}$	$743.43^{+152.87}_{-235.58}$	$1.47^{+0.58}_{-0.55}$	$13.81^{+3.07}_{-2.49}$	$557.75^{+178.53}_{-79.58}$	566.6	605.7
9	$(1.48\ ,\ 1.61)$	$0.54^{+0.06}_{-0.08}$	$475.3^{+\infty}_{-}$	$0.81^{+0.48}_{-0.69}$	$9.98^{+2.66}_{-2.11}$	$455.75^{+146.15}_{-126.86}$	476.7	515.8
10	$(1.61\ ,\ 1.73)$	$0.5^{+0.05}_{-0.08}$	$781.97^{+\infty}_{-}$	$0.94^{+0.48}_{-0.51}$	$8.44^{+1.84}_{-1.67}$	$531.33^{+87.4}_{-142.04}$	602.9	642.0
11	$(1.73\ ,\ 1.89)$	$0.65^{+0.06}_{-0.06}$	$101.37^{+24.15}_{-15.44}$	$1.13^{+0.19}_{-0.09}$	$14.66^{+3.53}_{-2.85}$	$497.77^{+142.0}_{-92.12}$	566.5	605.6
12	$(1.89\ ,\ 2.21)$	$0.97^{+0.05}_{-0.05}$	$112.34^{+19.34}_{-21.18}$	$1.47^{+0.2}_{-0.22}$	$27.19^{+5.16}_{-4.51}$	$762.17^{+517.69}_{-246.11}$	571.9	610.9
13	$(2.21\ ,\ 2.51)$	$0.85^{+0.05}_{-0.05}$	$621.38^{+\infty}_{-}$	$1.23^{+0.59}_{-0.81}$	$16.39^{+3.53}_{-3.22}$	$670.21^{+224.96}_{-140.12}$	545.8	584.9
14	$(2.51\ ,\ 2.60)$	$0.42^{+0.06}_{-0.06}$	$583.31^{+66.95}_{-57.78}$	$1.39^{+0.44}_{-0.45}$	$6.88^{+1.86}_{-1.52}$	$719.25^{+263.92}_{-154.81}$	541.4	580.5
15	$(2.60\ ,\ 2.72)$	$0.56^{+0.06}_{-0.05}$	$716.86^{+\infty}_{-122.16}$	$1.24^{+0.48}_{-0.47}$	$9.74^{+2.4}_{-1.93}$	$669.58^{+204.59}_{-117.41}$	635.7	674.8
16	$(2.72\ ,\ 2.86)$	$0.46^{+0.06}_{-0.06}$	$687.69^{+182.38}_{-118.26}$	$1.3^{+0.51}_{-0.5}$	$5.56^{+1.47}_{-1.18}$	$540.5^{+134.19}_{-84.18}$	562.2	601.3
17	$(2.86\ ,\ 3.05)$	$0.61^{+0.03}_{-0.03}$	$659.96^{+79.95}_{-68.66}$	$1.75^{+0.27}_{-0.21}$	$7.4^{+1.1}_{-0.97}$	$1000.0^{+\infty}_{-75.62}$	603.2	642.3
18	$(3.05\ ,\ 3.21)$	$0.48^{+0.03}_{-0.03}$	$591.72^{+93.09}_{-85.88}$	$1.03^{+0.13}_{-0.11}$	$4.47^{+0.74}_{-0.66}$	$1000.0^{+\infty}_{-386.19}$	836.4	875.5
19	$(3.21\ ,\ 3.39)$	$0.6^{+0.07}_{-0.03}$	$534.91^{+34.66}_{-34.13}$	$2.38^{+0.07}_{-0.07}$	$5.84^{+1.01}_{-0.91}$	$------$	618.5	657.6
20	$(3.39\ ,\ 3.58)$	$0.57^{+0.04}_{-0.05}$	$617.75^{+39.99}_{-38.23}$	$2.49^{+0.35}_{-0.45}$	$5.48^{+1.18}_{-1.07}$	$7184.06^{+\infty}_{-4767.06}$	632.7	671.8
21	$(3.58\ ,\ 3.77)$	$0.56^{+0.03}_{-0.03}$	$588.7^{+21.41}_{-31.56}$	$2.65^{+0.06}_{-0.13}$	$4.4^{+0.56}_{-0.69}$	$------$	729.7	768.8
22	$(3.77\ ,\ 3.89)$	$0.42^{+0.03}_{-0.04}$	$534.85^{+25.82}_{-26.59}$	$2.51^{+0.07}_{-0.07}$	$3.54^{+0.69}_{-0.61}$	$------$	689.2	728.3
23	$(3.89\ ,\ 3.99)$	$0.47^{+0.04}_{-0.04}$	$458.14^{+28.35}_{-26.61}$	$2.46^{+0.09}_{-0.14}$	$5.78^{+1.15}_{-0.97}$	$------$	730.0	769.1
24	$(3.99\ ,\ 4.10)$	$0.24^{+0.07}_{-0.08}$	$557.71^{+\infty}_{-}$	$0.58^{+0.48}_{-0.39}$	$2.7^{+0.89}_{-0.69}$	$437.47^{+115.05}_{-77.19}$	660.6	699.7
25	$(4.10\ ,\ 4.23)$	$0.37^{+0.07}_{-0.08}$	$436.99^{+158.91}_{-97.63}$	$0.98^{+0.47}_{-0.47}$	$4.25^{+1.32}_{-1.03}$	$501.82^{+189.98}_{-108.93}$	652.5	691.6
26	$(4.23\ ,\ 4.37)$	$0.51^{+0.07}_{-0.02}$	$213.93^{+10.02}_{-29.5}$	$1.21^{+0.4}_{-0.16}$	$8.87^{+1.89}_{-1.33}$	$471.94^{+139.7}_{-97.74}$	582.9	622.0
27	$(4.37\ ,\ 4.51)$	$0.71^{+0.07}_{-0.07}$	$313.09^{+145.24}_{-107.63}$	$1.34^{+0.52}_{-0.47}$	$19.69^{+5.27}_{-4.26}$	$471.09^{+237.63}_{-123.53}$	624.7	663.8
28	$(4.51\ ,\ 4.65)$	$0.88^{+0.05}_{-0.05}$	$417.43^{+42.94}_{-33.02}$	$2.77^{+0.43}_{-0.44}$	$35.19^{+6.78}_{-6.22}$	$3269.48^{+\infty}_{-1994.58}$	596.8	635.9
29	$(4.65\ ,\ 4.79)$	$0.69^{+0.04}_{-0.04}$	$424.23^{+14.82}_{-38.77}$	$2.04^{+0.23}_{-0.37}$	$14.96^{+2.83}_{-2.35}$	$1327.91^{+81.85}_{-451.3}$	640.5	679.6

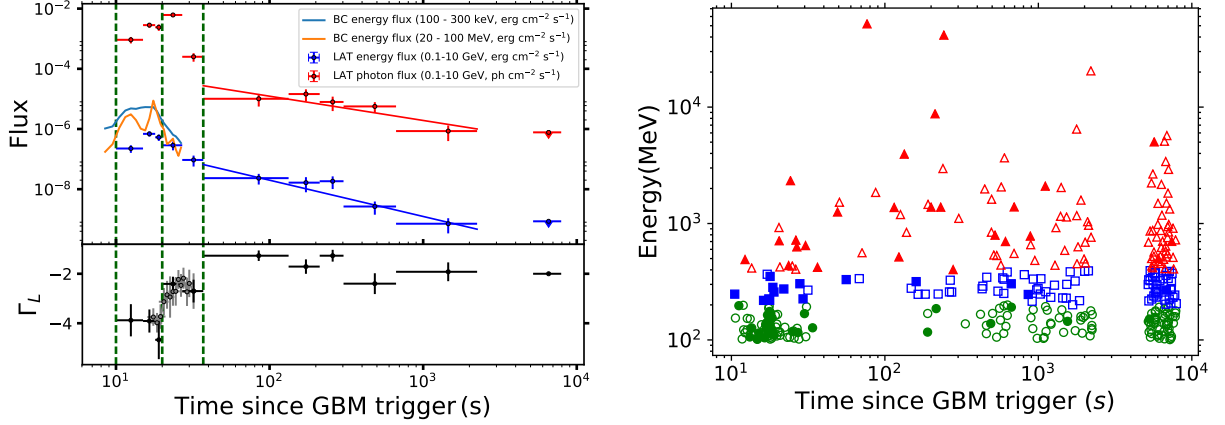| bkn2pow							$dof = 558$	
Sr. no.	(t_1,t_2)	α_1	E_1 (keV)	α_2	E_2 (keV)	β	K^b	AIC	BIC
1	$(-0.26\ ,\ 0.51)$	$0.97^{+0.03}_{-0.03}$	132^{+16}_{-11}	$1.59^{+0.16}_{-0.03}$	557^{+234}_{-86}	$2.79^{+0.51}_{-0.18}$	$11.08^{+2.02}_{-1.40}$	690.5	733.9
2	$(0.51\ ,\ 0.69)$	$0.72^{+0.05}_{-0.05}$	126^{+17}_{-21}	$1.45^{+0.13}_{-0.16}$	464^{+85}_{-71}	$2.93^{+0.35}_{-0.24}$	$14.80^{+3.15}_{-2.78}$	556.7	600.1
3	$(0.69\ ,\ 0.83)$	$0.69^{+0.05}_{-0.06}$	114^{+16}_{-18}	$1.42^{+0.12}_{-0.12}$	503^{+71}_{-60}	$2.92^{+0.28}_{-0.20}$	$16.28^{+3.81}_{-3.40}$	553.7	597.1
4	$(0.83\ ,\ 0.95)$	$0.69^{+0.04}_{-0.03}$	125^{+18}_{-9}	$1.44^{+0.15}_{-0.02}$	563^{+90}_{-33}	$3.36^{+0.45}_{-0.17}$	$18.25^{+2.68}_{-2.51}$	512.1	555.5
5	$(0.95\ ,\ 1.08)$	$0.70^{+0.04}_{-0.04}$	115^{+18}_{-11}	$1.40^{+0.16}_{-0.02}$	446^{+75}_{-46}	$2.94^{+0.26}_{-0.11}$	$19.38^{+3.38}_{-3.12}$	570.0	613.5
6	$(1.08\ ,\ 1.22)$	$0.74^{+0.05}_{-0.06}$	127^{+24}_{-21}	$1.49^{+0.14}_{-0.12}$	640^{+113}_{-78}	$3.29^{+0.45}_{-0.29}$	$20.99^{+4.77}_{-4.20}$	507.7	551.1
7	$(1.22\ ,\ 1.35)$	$0.78^{+0.05}_{-0.06}$	135^{+24}_{-25}	$1.33^{+0.09}_{-0.09}$	754^{+79}_{-69}	$3.68^{+0.45}_{-0.32}$	$23.41^{+4.90}_{-4.33}$	515.8	559.3
8	$(1.35\ ,\ 1.48)$	$0.75^{+0.04}_{-0.05}$	227^{+71}_{-53}	$1.41^{+0.20}_{-0.15}$	752^{+68}_{-69}	$3.61^{+0.38}_{-0.30}$	$20.09^{+3.77}_{-3.65}$	565.5	608.9
9	$(1.48\ ,\ 1.61)$	$0.66^{+0.03}_{-0.05}$	181^{+46}_{-37}	$1.39^{+0.18}_{-0.18}$	703^{+94}_{-104}	$3.57^{+0.49}_{-0.37}$	$14.05^{+2.14}_{-2.57}$	484.8	528.2
10	$(1.61\ ,\ 1.73)$	$0.61^{+0.05}_{-0.05}$	190^{+42}_{-33}	$1.26^{+0.11}_{-0.10}$	795^{+71}_{-53}	$3.57^{+0.31}_{-0.23}$	$11.39^{+2.49}_{-2.20}$	611.1	654.5
11	$(1.73\ ,\ 1.89)$	$0.73^{+0.05}_{-0.06}$	102^{+17}_{-11}	$1.51^{+0.14}_{-0.11}$	424^{+110}_{-57}	$2.77^{+0.30}_{-0.18}$	$18.12^{+4.29}_{-3.52}$	570.7	614.1
12	$(1.89\ ,\ 2.21)$	$1.02^{+0.04}_{-0.04}$	115^{+14}_{-13}	$1.79^{+0.10}_{-0.12}$	630^{+177}_{-176}	$3.17^{+1.04}_{-0.56}$	$31.29^{+5.61}_{-4.94}$	573.4	616.8
13	$(2.21\ ,\ 2.51)$	$0.91^{+0.04}_{-0.04}$	158^{+38}_{-36}	$1.38^{+0.12}_{-0.12}$	681^{+131}_{-74}	$3.13^{+0.42}_{-0.27}$	$19.04^{+3.44}_{-3.14}$	543.8	587.2
14	$(2.51\ ,\ 2.60)$	$0.44^{+0.06}_{-0.06}$	141^{+35}_{-27}	$0.91^{+0.10}_{-0.09}$	662^{+49}_{-42}	$3.30^{+0.20}_{-0.17}$	$6.95^{+1.97}_{-1.64}$	553.0	596.4
15	$(2.60\ ,\ 2.72)$	$0.58^{+0.06}_{-0.06}$	131^{+51}_{-19}	$1.06^{+0.11}_{-0.07}$	731^{+62}_{-51}	$3.24^{+0.23}_{-0.18}$	$9.68^{+2.70}_{-2.08}$	623.0	666.4
16	$(2.72\ ,\ 2.86)$	$0.62^{+0.04}_{-0.06}$	257^{+62}_{-81}	$1.33^{+0.23}_{-0.22}$	747^{+94}_{-79}	$3.60^{+0.42}_{-0.30}$	$9.07^{+1.90}_{-2.04}$	569.4	612.9
17	$(2.86\ ,\ 3.05)$	$0.72^{+0.03}_{-0.03}$	324^{+206}_{-123}	$1.05^{+1.69}_{-0.22}$	689^{+428}_{-64}	$3.05^{+0.41}_{-0.16}$	$10.82^{+1.80}_{-1.58}$	579.6	623.0
18	$(3.05\ ,\ 3.21)$	$0.56^{+0.06}_{-0.06}$	144^{+89}_{-44}	$0.76^{+0.09}_{-0.07}$	679^{+47}_{-44}	$2.57^{+0.085}_{-0.07}$	$5.67^{+1.59}_{-1.30}$	660.5	703.9
19	$(3.21\ ,\ 3.39)$	$0.47^{+0.06}_{-0.06}$	141^{+51}_{-25}	$0.83^{+0.09}_{-0.08}$	614^{+40}_{-40}	$2.43^{+0.074}_{-0.06}$	$3.55^{+1.04}_{-0.83}$	596.8	640.3
20	$(3.39\ ,\ 3.58)$	$0.57^{+0.03}_{-0.03}$	485^{+77}_{-114}	$1.69^{+0.46}_{-0.44}$	965^{+262}_{-122}	$3.04^{+0.18}_{-0.15}$	$5.49^{+1.01}_{-0.87}$	613.3	656.7
21	$(3.58\ ,\ 3.77)$	$0.52^{+0.03}_{-0.04}$	408^{+63}_{-59}	$1.46^{+0.33}_{-0.29}$	833^{+137}_{-100}	$2.82^{+0.14}_{-0.12}$	$3.77^{+0.73}_{-0.63}$	704.2	747.6
22	$(3.77\ ,\ 3.89)$	$0.28^{+0.09}_{-0.07}$	205^{+165}_{-55}	$0.85^{+0.57}_{-0.16}$	645^{+137}_{-51}	$2.59^{+1.87}_{-0.08}$	$0.99^{+0.05}_{-0.04}$	654.7	698.1
23	$(3.89\ ,\ 3.99)$	$0.22^{+0.07}_{-0.08}$	143^{+20}_{-20}	$0.95^{+0.10}_{-0.10}$	594^{+42}_{-39}	$2.62^{+0.09}_{-0.08}$	$2.12^{+0.75}_{-0.61}$	648.6	692.0
24	$(3.99\ ,\ 4.10)$	$0.35^{+0.06}_{-0.07}$	177^{+32}_{-34}	$1.10^{+0.13}_{-0.14}$	656^{+58}_{-49}	$3.18^{+0.20}_{-0.16}$	$3.66^{+1.10}_{-0.99}$	640.2	683.6
25	$(4.10\ ,\ 4.23)$	$0.50^{+0.06}_{-0.05}$	196^{+100}_{-35}	$1.16^{+0.50}_{-0.16}$	574^{+162}_{-50}	$3.04^{+0.24}_{-0.16}$	$6.27^{+1.90}_{-1.28}$	639.9	683.3
26	$(4.23\ ,\ 4.37)$	$0.64^{+0.06}_{-0.02}$	180^{+5}_{-22}	$1.66^{+0.18}_{-0.04}$	489^{+24}_{-64}	$3.15^{+0.33}_{-0.13}$	$13.14^{+1.17}_{-1.92}$	558.5	601.9
27	$(4.37\ ,\ 4.51)$	$0.81^{+0.04}_{-0.04}$	162^{+39}_{-22}	$1.48^{+0.29}_{-0.18}$	426^{+91}_{-52}	$2.93^{+0.33}_{-0.22}$	$25.87^{+4.99}_{-4.09}$	607.2	650.6
28	$(4.51\ ,\ 4.65)$	$0.90^{+0.03}_{-0.03}$	322^{+56}_{-55}	$1.88^{+0.62}_{-0.31}$	596^{+276}_{-76}	$3.50^{+1.11}_{-0.31}$	$36.83^{+5.10}_{-4.60}$	584.6	628.1
29	$(4.65\ ,\ 4.79)$	$0.75^{+0.02}_{-0.03}$	332^{+10}_{-42}	$1.94^{+0.12}_{-0.17}$	882^{+54}_{-39}	$3.95^{+0.42}_{-0.33}$	$18.06^{+1.91}_{-1.97}$	616.7	660.2

Figure 6. GRB 160509A : (*Left*), flux evolution in the energy band 0.1 - 10 GeV is shown. There are two distinct components in the LAT (> 100 MeV) emission, a fast varying (FV) prompt emission component and a slow varying (SV) afterglow component. The afterglow component is engraved into the prompt emission and is subdominant. The photon index smoothly changes from softer to harder values showing the transition from the FV to the SV component. *Right* The light curve in three different energy ranges is shown here. The filled data points are the photons that have $\geq 90\%$ probability of association with GRB 160509A and the open data-points are ones with probability $< 90\%$. Circles denote photons with energy between 100 MeV and 200 MeV, squares represent photons between 200 MeV and 400 MeV, and stars represent photons with energy > 400 MeV. The first photon with energy greater than 400 MeV (and thus spectrally lying on the harder power law) is at $T0 + 12.27$ s. It is coincident with the peak of the first LLE pulse (20-100 MeV). The second photon with a greater energy 711 MeV is at 20.5 s and coincident with the end of second LLE pulse. This point in time can be the beginning of a temporal component different from the prompt emission

REFERENCES

Abdo, A. A., Ackermann, M., Asano, K., et al. 2009, ApJ, 707, 580

Ackermann, M., Ajello, M., Asano, K., et al. 2013, ApJS, 209, 11

Acuner, Z., Ryde, F., Pe'er, A., Mortlock, D., & Ahlgren, B. 2020, arXiv e-prints, arXiv:2003.06223

Ahlgren, B., Larsson, J., Valan, V., et al. 2019, ApJ, 880, 76

Arnaud, K. A. 1996, in Astronomical Society of the Pacific Conference Series, Vol. 101, Astronomical Data Analysis Software and Systems V, ed. G. H. Jacoby & J. Barnes, 17

Atwood, W. B., Baldini, L., Bregeon, J., et al. 2013, ApJ, 774, 76

Axelsson, M., Baldini, L., Barbiellini, G., et al. 2012, ApJL, 757, L31

Band, D., Matteson, J., Ford, L., et al. 1993, ApJ, 413, 281

Basak, R., & Rao, A. R. 2013, ApJ, 768, 187

—. 2015, ApJ, 812, 156

Beloborodov, A. M., & Mészáros, P. 2017, Space Science Reviews, 207, 87. https://doi.org/10.1007/s11214-017-0348-6

Burgess, J. M. 2019, A&A, 629, A69

Burgess, J. M., Bégué, D., Bacelj, A., et al. 2018, arXiv e-prints, arXiv:1810.06965

Castro-Tirado, A. J., Hu, Y., Fernandez-Garcia, E., et al. 2019, GRB Coordinates Network, 23708, 1

de Jager, O. C., & Harding, A. K. 1992, ApJ, 396, 161

Fraija, N., Dichiara, S., Pedreira, A. C. C. d. E. S., et al. 2019, ApJL, 879, L26

Frederiks, D., Golenetskii, S., Aptekar, R., et al. 2019, GRB Coordinates Network, 23737, 1

Gill, R., & Granot, J. 2018, MNRAS, 475, L1

Guilbert, P. W., Fabian, A. C., & Rees, M. J. 1983, MNRAS, 205, 593

Guiriec, S., Mochkovitch, R., Piran, T., et al. 2015a, ApJ, 814, 10

Guiriec, S., Connaughton, V., Briggs, M. S., et al. 2011, ApJL, 727, L33

Guiriec, S., Daigne, F., Hascoët, R., et al. 2013, ApJ, 770, 32

Guiriec, S., Kouveliotou, C., Daigne, F., et al. 2015b, ApJ, 807, 148

Guiriec, S., Kouveliotou, C., Hartmann, D. H., et al. 2016, ApJL, 831, L8

Gupta, N., & Zhang, B. 2008, MNRAS, 384, L11

Iyyani, S., Ryde, F., Axelsson, M., et al. 2013, MNRAS, 433, 2739

Kass, R. E., & Rafferty, A. E. 1995, J. Am. Stat. Assoc., 90, 773

Koshut, T. M., Paciesas, W. S., Kouveliotou, C., et al. 1995, in American Astronomical Society Meeting Abstracts, Vol. 186, American Astronomical Society Meeting Abstracts #186, 53.01

Kumar, P., & Zhang, B. 2015, PhR, 561, 1

Li, L. 2019a, arXiv e-prints, arXiv:1905.02340

—. 2019b, ApJS, 242, 16

Lithwick, Y., & Sari, R. 2001, ApJ, 555, 540

Lyutikov, M., & Blandford, R. 2003, arXiv e-prints, astro

MAGIC Collaboration, Acciari, V. A., Ansoldi, S., et al. 2019, Nature, 575, 459

Mirzoyan, R., Noda, K., Moretti, E., et al. 2019, GRB Coordinates Network, 23701, 1

Narayan, R., & Kumar, P. 2009, MNRAS, 394, L117

Oganesyan, G., Nava, L., Ghirlanda, G., & Celotti, A. 2017a, ApJ, 846, 137

—. 2017b, ArXiv e-prints, arXiv:1710.09383

—. 2017c, ApJ, 846, 137

Oganesyan, G., Nava, L., Ghirlanda, G., Melandri, A., & Celotti, A. 2019, A&A, 628, A59

Page, K. L., Starling, R. L. C., Fitzpatrick, G., et al. 2011, MNRAS, 416, 2078

Pe'er, A., Ryde, F., Wijers, R. A. M. J., Mészáros, P., & Rees, M. J. 2007, ApJL, 664, L1

Piran, T., & Nakar, E. 2010, ApJ, 718, L63

Ravasio, M. E., Ghirlanda, G., Nava, L., & Ghisellini, G. 2019a, A&A, 625, A60

Ravasio, M. E., Oganesyan, G., Salafia, O. S., et al. 2019b, arXiv e-prints, arXiv:1902.01861

Ryde, F. 2005, ApJL, 625, L95

Tang, Q.-W., Peng, F.-K., Wang, X.-Y., & Tam, P.-H. T. 2015, ApJ, 806, 194

Ursi, A., Tavani, M., Marisaldi, M., et al. 2019, GRB Coordinates Network, 23712, 1

Vianello, G., Gill, R., Granot, J., et al. 2017, ArXiv e-prints, arXiv:1706.01481

Vurm, I., & Beloborodov, A. M. 2016, ApJ, 831, 175

Wang, Y., Li, L., Moradi, R., & Ruffini, R. 2019, arXiv e-prints, arXiv:1901.07505

Wang, Y.-Z., Wang, H., Zhang, S., et al. 2017, ApJ, 836, 81

Zhang, B., & Pe'er, A. 2009, ApJL, 700, L65

Zhang, B.-B., Uhm, Z. L., Connaughton, V., Briggs, M. S., & Zhang, B. 2016, ApJ, 816, 72

Zhang, B.-B., Zhang, B., Castro-Tirado, A. J., et al. 2018, Nature Astronomy, 2, 69